Broadband acoustic silencer with ventilation based on slit-type Helmholtz resonators

Huy Nguyen, Qian Wu, Xianchen Xu, Hui Chen, Sharon Tracy ⓘ, and Guoliang Huang ⓘ

View Online   Export Citation   CrossMark

Broadband acoustic silencer with ventilation based on slit-type Helmholtz resonators

Huy Nguyen,[1] Qian Wu,[1] Xianchen Xu,[1] Hui Chen,[1] Sharon Tracy,[2] (iD) and Guoliang Huang[1,a] (iD)

AFFILIATIONS

[1]Department of Mechanical and Aerospace Engineering, University of Missouri, Columbia, Missouri 65211, USA
[2]Materials Innovation, Steelcase Inc., Grand Rapids, Michigan 49508, USA

[a]Author to whom correspondence should be addressed: huangg@missouri.edu

ABSTRACT

Recently, sound attenuation with ventilation is highly needed in many practical applications. In this study, we report on a subwavelength acoustic silencer, named double-layer acoustic silencer (DAS), based on compactly assembled slit-type Helmholtz resonators (SHRs) for low-frequency broadband sound insulation while preserving ventilation. A simple yet insightful theoretical model is first established to characterize the sound insulation performance in terms of transmission loss (TL) and used for microstructure designs of the DAS. The fluctuating TL of the DAS, inevitably produced by the SHR resonances, is then mitigated and optimized via the introduction of viscosity and proper SHR frequency detuning. The overall TL is numerically investigated and experimentally observed to reach beyond 30 dB over the target working band of 0.48–0.95 kHz, with a maximum exceeding 50 dB. In addition, the proposed design also provides perfect ventilation when deployed in a duct environment, due to the straight and conserved airflow cross section. We believe that the proposed acoustic silencer design and its associated theoretical model pave the way for designing and optimizing highly efficient low-frequency subwavelength acoustic liners and silencers.

Conventional airborne sound attenuation essential in acoustic barriers refers to either reflecting or absorbing the incident acoustic energy while blocking airflow transport. The modern demand for sound attenuation, while preserving ventilation, such as the applications of mitigating engine and office noise, has prompted considerable effort put to the research of duct acoustics.[1–4] Among the existing works, Herschel–Quincke waveguides[5–7] are notable, as the narrow-band sound attenuation can be achieved with minimal reduction in the duct airflow area. Although these classical designs indeed provide simultaneous sound attenuation and ventilation, their inherent in-duct nature, along with their large physical footprint, limits the versatility and practical implementation. In practice, a more winding lined path supports a more prominent noise reduction, which in turn results in a larger pressure drop and a poorer ventilation effect. Hence, there has always been a trade-off between the efficiency of ventilation and the noise reduction. Acoustic local resonators have been widely studied in various noise control environments for low-frequency noise reduction. Typical applications include sound diffusers and absorbers in room acoustics,[8–11] improvement of sound transmission loss (TL) of aircraft sidewalls,[12] acoustic metamaterials,[13,14] and so forth. Among them, purely acoustic resonators like Helmholtz and Fabry–Pérot

resonators are most employed due to their high Q-factors[2] and simple structures. Recently, acoustic local resonators were also utilized as side branches in ducts or pipes in order to mitigate the sound transmission inside waveguides.[15–17] However, strong TL across broadband is still difficult to be achieved in the subwavelength regime, owing to the existence of strong antiresonances.[15,18,19] Meanwhile, the restriction on the gradient length of the coiled channel resonators often leads to practical challenges in assembling multiple functional units for the realization of broadband absorption and attenuation.[16,17,20,21] Moreover, in the acoustic barrier designs,[16,17,22] the local acoustic resonators are immersed in the airflow to achieve high transmission loss. However, the smaller working cross-sectional area and discontinuous airflow inevitably result in a lower ventilation efficiency.

To address the aforementioned issues, we theoretically investigate and experimentally validate a subwavelength double-layer acoustic silencer (DAS) composed of multiple slit-type Helmholtz resonators (SHRs), possessing subwavelength slit necks and enabling broadband TL and effective air ventilation. The DAS is constructed with two compactly assembled single-layer acoustic silencers (SASs) to enhance the broadband sound insulation performance. Such an acoustic barrier effectively blocks over 99.9% of the incident sound energy over a

broadband frequency range of 0.48–0.95 kHz while maintaining excellent ventilation due to the straight and conserved airflow cross section. In the theoretical part, we derive a comprehensive analytical model for the individual SHR, together with its derivatives, namely, the SAS and the DAS, to gain better understanding of the involved physical mechanism. The corresponding numerical and experimental results effectively support the developed theory with excellent agreement between them. Finally, we strongly believe that our work uncovers the fundamental characteristics of the slit-type Helmholtz resonators and may pave the way for designing highly efficient subwavelength acoustic silencers with broadband operation and great tunability.

We start by designing a slit-type Helmholtz resonator (SHR), which serves as the building block of the compact acoustic silencer. Figure 1(a) provides the sectional view of the three-dimensional (3D) model of a side-branched SHR. The SHR is axisymmetric and consists of a cavity and a slit neck. Due to the massive friction area inside the neck, the dissipated energy via the thermal viscosity is expected to be significantly amplified. Both the resonance frequency of the SHR and the thermal viscosity can be tuned flexibly by varying the slit thickness and the cavity depth. Figure 1(b) illustrates the schematic of a single SHR with all the geometric parameters denoted for the complete theoretical analysis. Due to the complex geometry of the SHR, in the theoretical modeling, we divide the SHR into four domains (cavity A and necks B, C, and D). The acoustic impedance of the SHR is derived using a backtracking procedure (see the supplementary material). The acoustic impedance at the inlet of the SHR reads
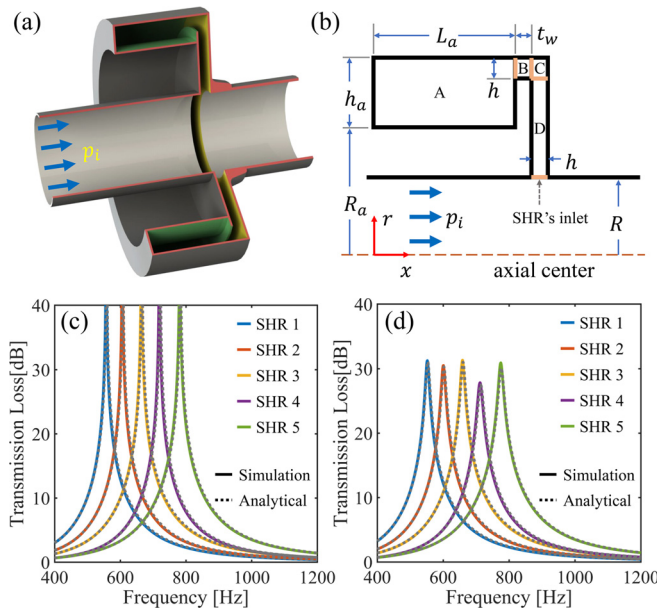
FIG. 1. (a) Sectional view of a side-branched SHR. The blue arrows correspond to the incoming acoustic waves. (b) Schematic of a SHR with all the involved geometrical parameters indicated. The SHR is divided into multiple domains, labeled as A, B, C, and D. (c) and (d) TL spectra of non-viscous and viscous SHRs, respectively. The dashed curves correspond to analytical results, whereas the solid ones represent the simulation results.

$$Z_h = -i\rho_d c_d \frac{J_0(kR) - \alpha_d Y_0(kR)}{J_1(kR) - \alpha_d Y_1(kR)}, \tag{1}$$

where ρ_d and c_d are the mass density and sound velocity inside domain D, respectively. J_n and Y_n are the nth order Bessel function of the first and second kinds; the wavefunction factor α_d is determined from the acoustic impedance at the boundary between domains C and D. When the thermal viscosity is considered, the released energy through heat mainly occurs inside the neck at resonant frequencies, since the velocity inside the SHR reaches maximum due to the abrupt reduction of the cross-sectional area at the ends of the neck. For the slit-type neck, effective mass density (ρ_e) and sound velocity (c_e) are considered,[23] taking into account the thermal viscous effect,

$$\rho_e = \frac{\rho}{\phi_v} \quad \text{and} \quad c_e = c\sqrt{\frac{\phi_v}{\gamma - (\gamma - 1)\phi_h}}, \tag{2}$$

where ρ, c, and γ are the mass density, sound velocity, and ratio of specific heat of air, respectively. ϕ_v and ϕ_h are viscosity-geometry and thermal-geometry functions for slits (see the supplementary material). Being side-branched to a duct and under an external excitation, the air layer at the inlet oscillates and radiates energy back into the upstream and downstream of the duct symmetrically. The SHR, therefore, performs as a monopole. The radiation field comprises far-field and near-field components. The far-field component is induced by the fundamental mode and conserved while propagating outward, whereas the near-field component is produced by the higher-order modes of the duct and decays exponentially away from the inlet. Thus, the far-field component represents losing energy and its corresponding specific impedance is purely resistive.[2] The energy carried by the near-field component, in contrast, is preserved and oscillates in the vicinity of the inlet. Its corresponding impedance is purely reactive.[10,24] Aside from the impedance at the inlet, the input impedance of the SHR, therefore, needs to be taken into consideration for the radiation impedance, denoted as

$$Z_{in} = Z_h + \mathbb{R} - i\chi, \tag{3}$$

in which $\mathbb{R}$ and χ are the resistance and mass reactance corresponding to the far-field radiation and the near-field component, respectively. For traditional Helmholtz resonators, $\mathbb{R} = \sigma\rho c/2$ and χ can be approximately estimated through neck length correction.[25] However, due to the complicated geometry of the SHR attached to a duct, we employ Green's function method to evaluate $\mathbb{R}$ and χ (see the supplementary material). $Z_h^{(cr)} = Z_h - i\chi$ is the corrected specific acoustic impedance of the SHR.[24] The resonances of the SHR are then determined under the condition of zero reactance of the corrected specific impedance (Img$\{Z_h\} = \chi$). It is noteworthy that for the non-viscous SHR, Z_h is purely imaginary (reactive). The resonant frequencies of the side-branched SHR are lower than those of an isolated SHR whose resonances are determined from the condition Img$\{Z_h\} = 0$ because $\chi < 0$ and Img$\{Z_h\}$ are characterized by a positive-slope curve. The transmission and reflection coefficients of the side-branched SHR then read

$$T_h = 1 - \frac{\mathbb{R}}{\mathbb{R} + Z_h^{(cr)}} \quad \text{and} \quad R_h = -\frac{\mathbb{R}\nu^2}{\mathbb{R} + Z_h^{(cr)}}, \tag{4}$$

respectively, where $\nu^2 = e^{-2ikx_h}$ is the reflection phase shifting term and x_h is the coordinate of the SHR inlet. One can clearly see $T_h - R_h = 1$, which completely differs from the case of the thin

membrane,[26,27] i.e., $T_h + R_h = 1$. This is due to the fact that the continuous air pressure field inside the duct leads to the in-phase T_h and R_h, while in the thin membrane scenario, T_h and R_h are out-of-phase.

For a lossless side-branched SHR mounted on the duct, its radiating pressure fields at the resonances in the downstream possess the same amplitudes as the incident pressure field, but are out of phase, leading to TL peaks (TL $= -20 \log_{10} |T_h|$). This observation is readily confirmed by Eq. (4), showing that $T_h = 0$ when $Z_h^{(cr)} = 0$. In general, such a SHR possesses multiple resonances. The first resonance, which happens to be the strongest with the lowest frequency, gives the largest TL along with the highest Q-factor. In this work, we focus only on the first SHR resonance.

Five SHRs with different geometrical parameters are assembled compactly to form a subwavelength single-layer acoustic silencer (SAS), as illustrated in Fig. 2(a). They are designed such that their working frequencies are distributed evenly within the working band of 0.5–1 kHz. Conducting a parametric study using the numerical software COMSOL Multiphysics allows us to determine the optimal geometrical parameters of each SHR, see Table I. To simplify the numerical model, the thicknesses of all SHRs are set as $t_w = 1$ mm, which is feasible for 3D printing. The TL spectra of the non-viscous and viscous SHRs are calculated numerically and analytically, as presented in Figs. 1(c) and 1(d), respectively. Great agreement can be visualized between the theoretical prediction and the simulations,

TABLE I. The dimensions of the individual SHRs.

	First SHR	Second SHR	Third SHR	Fourth SHR	Fifth SHR
t_w(mm)	1.0	1.0	1.0	1.0	1.0
R_a(mm)	65.5	58.0	49.0	39.5	23.5
h_a(mm)	6.0	6.5	8.0	8.5	15.0
L_a(mm)	58.5	52.5	48.5	44.5	40.5
h(mm)	4.3	4.0	4.0	3.0	3.0

indicating that the developed theoretical model of the single SHR is reliable for the design and optimization purposes.

Since the necks of the SHRs within a SAS are subwavelength and compactly stacked (24.3 mm, less than $\lambda/14$ at 1 kHz), there may exist a near-field interaction between adjacent SHRs. The SAS, therefore, cannot be treated as a combination of isolated SHRs connected in parallel. To take into account the interaction, Green's function method is again employed, and the resultant transmission and reflection coefficients take the following matrix forms:

$$T = 1 - \frac{1}{2}\sum_{n=1}^{5}\sum_{m=1}^{5}(\sigma_n \alpha_n \nu_n^{-1})[\mathbf{F}^{-1}]_{nm}(\alpha_m \nu_m),\qquad(5)$$

$$R = -\frac{1}{2}\sum_{n=1}^{5}\sum_{m=1}^{5}(\sigma_n \alpha_n \nu_n^{-1})[\mathbf{F}^{-1}]_{nm}(\alpha_m \nu_m).\qquad(6)$$

Here, $\sigma_n = S_{dn}/S_0$, $\alpha_n = \sin(kh_n/2)/(kh_n/2)$, and $\nu_n = e^{-ikx_n}$, in which S_{dn}, h_n, and x_n denote the cross-sectional area, height, and coordinate of the nth SHR inlet, respectively. $\mathbf{F}$ is the coupling impedance matrix (see the supplementary material). The calculated TL profiles of the non-viscous and the viscous SASs, plotted in Fig. 2(c), show great agreement between the developed analytical solution [Eqs. (5) and (6)] and simulation results. For the non-viscous SAS, the TL peaks slightly shift, compared to the TL peaks of individual SHRs, due to the weak interaction between the adjacent SHRs (see the supplementary material). In addition, the TL outside the resonance region is significantly enhanced, which can be explained by the additive property of the coupling of adjacent slit necks in the non-resonant region. Within the resonant region, the dips lying between two adjacent TL peaks indicate TL even lower than those of the individual SHRs at the same frequency, owing to the Fano resonance induced by the coupling mainly between two adjacent SHR resonances.[28,29]

Since the existence of sharp dips causes a nonoptimal TL profile, we introduce high viscosity into the SHRs to make the TL profile less fluctuating. Because of the abrupt change in the cross-sectional areas of the neck inlet and the neck outlet, the velocity fields inside are strong at the resonances, leading to large slipping velocity fields between the air layers inside the viscous boundary layer. The massive friction area of the neck, therefore, guarantees a huge amount of acoustic energy to be released through the heat induced from the friction force between the slipping air layers. As a result, the peaks or the dips caused by the resonances become less sharp. The effect of the introduced viscosity on the TL performance can be seen directly from Fig. 1(d) for the SHRs and Fig. 2(c) for the SAS. Far away from the resonances, where the slipping velocity fields are weak, the effect of the
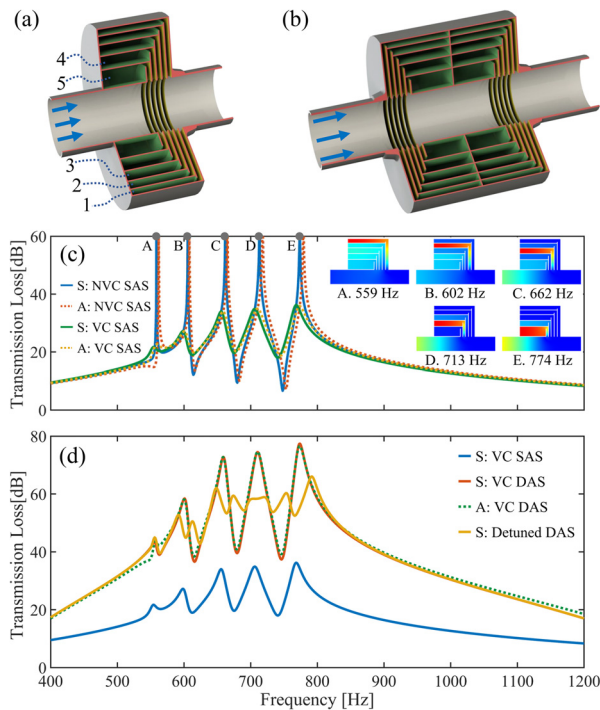
FIG. 2. (a) and (b) Sectional views of a single-layer acoustic silencer consisting of five labeled SHRs and the double-layer acoustic silencer containing two single-layer acoustic silencers. (c) TL spectra of the non-viscous (NVC) and viscous (VC) single-layer acoustic silencers from analytical and numerical calculations. (d) Comparison between the viscous single-layer and double-layer silencers and the detuned viscous double-layer silencer. Here, S and A correspond to simulation and analytical results, respectively.

viscosity is negligible. Within the resonance region, the influence of the viscosity is maximized.

To further improve the sound insulation performance, two SASs are compactly assembled to form a double-layer acoustic silencer (DAS), as illustrated in Fig. 2(b), which in theory doubles the overall TL of the SAS. This prediction is confirmed by Fig. 2(d) for both the non-viscous and the viscous cases. (The TL deteriorates as the two SASs are brought closer due to the emergence of non-negligible SHR couplings, see also the supplementary material.) To interpret this, we treat the two SASs as two acoustic impedance layers, separated by L_e, whose transmission and reflection coefficients are denoted by (T_1 and T_2) and (R_1 and R_2), respectively. In this way, the total transmission and the total reflection coefficients, respectively, take the forms

$$T = (v_e T_1 T_2)/(1 - R_1 R_2 v_e^2), \tag{7}$$

$$R = R_1 + (T_1^2 R_2 v_e^2)/(1 - R_1 R_2 v_e^2), \tag{8}$$

where $v_e = e^{-ikL_e}$. The effectiveness of Eqs. (7) and (8) is validated in the supplementary material. The TL reaches its maxima when $|T_1| \to 0$ or $|T_2| \to 0$, corresponding to the SAS resonance frequencies. It is implied that the SAS and the DAS are expected to exhibit TL peaks at the same frequencies. Moreover, when identical SASs, namely, $T_1 = T_2$ and $R_1 = R_2$, are chosen, the magnitude of the transmission reads $|T| = |T_1|^2/|1 - (v R_1)^2|$. The TL of the DAS is then approximated, in the vicinity of the resonances, as $2\mathrm{TL}_{SAS} + 20\log_{10}4\pi L/\lambda$ and around the antiresonances ($T \approx 1$) as $\mathrm{TL}_{DAS} \approx 2\mathrm{TL}_{SAS}$, which clearly suggests that TL_{DAS} is at least twice as high as TL_{SAS}. Although the DAS dramatically improves the sound insulation performance, the occurrence of the fluctuating TL profile still remains unsolved, even in the presence of strong viscosity. To address this issue, we slightly detune the resonance frequencies of the SHRs by shifting their separations by 3.5 mm. Consequently, additional peaks and dips appear. Although the detuning suppresses the TL around the resonances, the TL performance is improved overall to be at least 40 dB over the frequency range of 0.54–0.88 kHz. As for the ventilation efficiency, since the proposed designs support the straight airflow path with a constant cross section, the ventilation remains perfect even in the presence of the DAS (see the supplementary material for more information about air flow simulations).

To experimentally examine the viscous, detuned DAS design, we build the test bed shown in Fig. 3(a). The detuned DAS sample [see the inset of Fig. 3(a)] is fabricated from nylon using a Formlabs 3D printer. To ease the printing difficulty, we divide the DAS sample into six pieces and print them separately. The final DAS sample is then assembled by gluing all six pieces. Since both the theoretical and the simulation models assume the acoustically rigid shells of the silencer, the DAS is reinforced by thin supporting walls at the middle plane of each piece. The inner and outer diameters and the total length of the fabricated DAS are 44.5 mm, 145 mm, and 130 mm, respectively. This silencer, thus, can be considered as an acoustically subwavelength device compared with the working wavelength of 490 mm at the working band center (0.7 kHz). As shown in Fig. 3(b), the experimental measurement is in good agreement with the corresponding numerical simulation. The TL is observed to be greater than 20 dB across a broadband covering 0.43–1.1 kHz. More importantly, within the range of 0.48–1 kHz, the TL exceeds 30 dB with the maximum over 50 dB, proving excellent sound insulation performance. The deviation
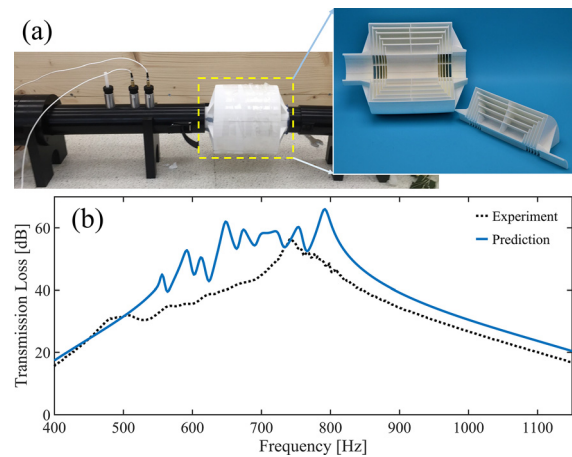
FIG. 3. (a) Photograph of the experimental setup including a Mecanum Inc. standard impedance tube and a detuned double-layer acoustic silencer sample (see the inset). (b) Comparison between the numerical (solid curve) and the experimental results (dashed curve) of the detuned double-layer acoustic silencer design.

between the experimental and the numerical results may originate from the imperfect assembling of DAS pieces, which leads to the acoustic leakage from the DAS to the tube and the weak acoustic interaction between adjacent DAS pieces. These imperfections weaken the pressure intensity inside the SHRs at their resonance frequencies, resulting in the smooth curve instead of the fluctuating profile shown in simulations. Furthermore, the working band could be broadened by adjusting the geometrical parameters of the SHRs or by packing more SHRs. It has been reported that the working band can become much broader if the first-order and the second-order resonances are brought close.[20] Due to the challenging control of both the fundamental and higher-order resonances in such a passive resonator, this work is, hence, focused only on exploring the first-order resonances of the SHRs.

Based on the slit-type Helmholtz resonators, we have designed and demonstrated a compact subwavelength acoustic silencer, named double-layer acoustic silencer, which realizes strong acoustic insulation applications over the broadband of 0.48–0.95 kHz while preserving perfect ventilation. All the involved structures have been studied analytically using a complete theoretical model. The simulations and experiments of this double-layer acoustic silencer show excellent broadband sound insulation performance: the transmission loss, serving as the measure of the sound insulation performance, maintains at least 20 dB over the range of 0.43–1.1 kHz, even greater than 30 dB within the region of 0.48–0.95 kHz, and reaches the maximum exceeding 50 dB. The overall transmission loss across the working band has been optimized by introducing additional viscosity and detuning the frequencies of the individual slit-type Helmholtz resonators. The proposed designs, supporting straight airflow path with a constant cross section, can maintain the excellent ventilation when deployed in a duct environment. Finally, our proposed subwavelength compact acoustic silencer paves the way toward the related future sound insulation devices.

See the supplementary material for the complete theoretical derivation and airflow simulations.

AUTHORS' CONTRIBUTIONS

H.N. and Q.W. contributed equally to this work.

DATA AVAILABILITY

The data that support the findings of this study are available from the corresponding author upon reasonable request.

REFERENCES

[1]R. E. Motsinger and R. E. Kraft, "Design and performance of duct acoustic treatment," in *Aeroacoustics of Flight Vehicles: Theory and Practice, NASA Ref. Pub. 1258* (NASA, Washington, DC, 1991), Vol. 2, pp. 165–206.

[2]T. Lee, T. Nomura, and H. Iizuka, "Damped resonance for broadband acoustic absorption in one-port and two-port systems," Sci. Rep. **9**, 13077 (2019).

[3]A. Merkel, G. Theocharis, O. Richoux, V. Romero-García, and V. Pagneux, "Control of acoustic absorption in one-dimensional scattering by resonant scatterers," Appl. Phys. Lett. **107**, 244102 (2015).

[4]U. Ingard, *Noise Reduction Analysis* (Jones & Bartlett Publishers, 2009).

[5]B. Poirier, C. Maury, and J.-M. Ville, "The use of Herschel-Quincke tubes to improve the efficiency of lined ducts," Appl. Acoust. **72**, 78–88 (2011).

[6]B. Poirier, J. M. Ville, C. Maury, and D. Kateb, "Bicylindrical model of Herschel-Quincke tube-duct system: Theory and comparison with experiment and finite element method," J. Acoust. Soc. Am. **126**, 1151–1162 (2009).

[7]R. Burdisso and J. Smith, "Control of inlet noise from turbofan engines using Herschel-Quincke waveguides," in 6th Aeroacoustics Conference Exhibit (2000).

[8]T. J. Cox and P. D'antonio, *Acoustic Absorbers and Diffusers: Theory, Design and Application* (CRC Press, 2009).

[9]U. Ingard, "On the theory and design of acoustic resonators," J. Acoust. Soc. Am. **25**, 1037–1061 (1953).

[10]D.-Y. Maa, "Potential of microperforated panel absorber," J. Acoust. Soc. Am. **104**, 2861–2866 (1998).

[11]Y. Zhu, X. Fan, B. Liang, J. Cheng, and Y. Jing, "Ultrathin acoustic metasurface-based Schroeder diffuser," Phys. Rev. X **7**, 021034 (2017).

[12]A. Selamet and I. Lee, "Helmholtz resonator with extended neck," J. Acoust. Soc. Am. **113**, 1975–1985 (2003).

[13]Z. Yang, J. Mei, M. Yang, N. H. Chan, and P. Sheng, "Membrane-type acoustic metamaterial with negative dynamic mass," Phys. Rev. Lett. **101**, 204301 (2008).

[14]N. Fang, D. Xi, J. Xu, M. Ambati, W. Srituravanich, C. Sun, and X. Zhang, "Ultrasonic metamaterials with negative modulus," Nat. Mater. **5**, 452–456 (2006).

[15]S.-H. Seo and Y.-H. Kim, "Silencer design by using array resonators for low-frequency band noise reduction," J. Acoust. Soc. Am. **118**, 2332–2338 (2005).

[16]M. Sun, X. Fang, D. Mao, X. Wang, and Y. Li, "Broadband acoustic ventilation barriers," Phys. Rev. Appl. **13**, 044028 (2020).

[17]R. Ghaffarivardavagh, J. Nikolajczyk, S. Anderson, and X. Zhang, "Ultra-open acoustic metamaterial silencer based on Fano-like interference," Phys. Rev. B **99**, 024302 (2019).

[18]Y. Cheng, C. Zhou, B. Yuan, D. Wu, Q. Wei, and X. Liu, "Ultra-sparse metasurface for high reflection of low-frequency sound based on artificial Mie resonances," Nat. Mater. **14**, 1013–1019 (2015).

[19]X. Zhu, B. Liang, W. Kan, Y. Peng, and J. Cheng, "Deep-subwavelength-scale directional sensing based on highly localized dipolar mie resonances," Phys. Rev. Appl. **5**, 054015 (2016).

[20]M. Yang, S. Chen, C. Fu, and P. Sheng, "Optimal sound-absorbing structures," Mater. Horiz. **4**, 673–680 (2017).

[21]S. Chen, Y. Fan, F. Yang, Y. Jin, Q. Fu, J. Zheng, and F. Zhang, "Engineering coiling-up space metasurfaces for broadband low-frequency acoustic absorption," Phys. Status Solidi RRL **13**, 1900426 (2019).

[22]H.-L. Zhang, Y.-F. Zhu, B. Liang, J. Yang, J. Yang, and J.-C. Cheng, "Omnidirectional ventilated acoustic barrier," Appl. Phys. Lett. **111**, 203502 (2017).

[23]M. R. Stinson, "The propagation of plane sound waves in narrow and wide circular tubes, and generalization to uniform tubes of arbitrary cross-sectional shape," J. Acoust. Soc. Am. **89**, 550–558 (1991).

[24]Y. Li, S. Qi, and M. B. Assouar, "Theory of metascreen-based acoustic passive phased array," New J. Phys. **18**, 043024 (2016).

[25]L. E. Kinsler, A. R. Frey, A. B. Coppens, and J. V. Sanders, *Fundamentals of Acoustics* (John Wiley & Sons, New York, 2000).

[26]Y. Chen, G. Huang, X. Zhou, G. Hu, and C.-T. Sun, "Analytical coupled vibroacoustic modeling of membrane-type acoustic metamaterials: Membrane model," J. Acoust. Soc. Am. **136**, 969–979 (2014).

[27]H. Nguyen, R. Zhu, J. K. Chen, S. L. Tracy, and G. L. Huang, "Analytical coupled modeling of a magneto-based acoustic metamaterial harvester," Smart Mater. Struct. **27**, 055010 (2018).

[28]Y. S. Joe, A. M. Satanin, and C. S. Kim, "Classical analogy of Fano resonances," Phys. Scr. **74**, 259–266 (2006).

[29]A. E. Miroshnichenko, S. Flach, and Y. S. Kivshar, "Fano resonances in nano-scale structures," Rev. Mod. Phys. **82**, 2257–2298 (2010).